Dennis Gabor: The father of seismic attribute analysis

Brian Russell[1]

[1] Hampson-Russell, A CGGVeritas Company, Calgary, Alberta, brian.russell@cggveritas.com

ABSTRACT

A review of the CREWES reports over the last ten years will reveal the influence of the Gabor transform on the work of Gary Margrave (e.g. Margrave et al., 2002), who has used this transform, along with his colleagues and students, to perform seismic deconvolution and migration. However, it is interesting to note that the Gabor transform was only one of three remarkable inventions in Gabor's landmark 1946 paper: "Theory of Communication", the others being time-frequency analysis and the complex signal. In this report, I will first give a brief discussion of time-frequency analysis and the Gabor transform, and then I will focus on Gabor's work on the complex signal and the development of seismic attribute analysis, trying to show the link among all seismic attributes. In this way, I will show that Gabor could be considered to be the "father" of seismic attribute analysis.

INTRODUCTION

Dennis Gabor was a Hungarian/British physicist who invented holography, for which he received the 1971 Nobel prize. In 1946, he also wrote one of the most influential papers of the 20th century, entitled: "Theory of communication". In that paper, he invented the complex signal, the Gabor transform and time-frequency analysis, each of which has had a major impact on our profession. In this report, I will discuss on how his development of the complex signal lead to seismic attribute analysis. But first, I will briefly review his work on the Gabor transform and time-frequency analysis.

Let us first review the Fourier transform, $S(\omega)$, of a seismic signal $s(t)$, which is written in continuous form as

$$S(\omega) = \frac{1}{\sqrt{2\pi}} \int_{-\infty}^{\infty} s(t) e^{-i\omega t} dt \ , \tag{1}$$

where $\omega = 2\pi f$, f = frequency and $i = \sqrt{-1}$. The inverse Fourier transform is written

$$s(t) = \frac{1}{\sqrt{2\pi}} \int_{-\infty}^{\infty} S(\omega) e^{i\omega t} d\omega \, . \tag{2}$$

In equations (1) and (2) note that the seismic signal $s(t)$ is real but that the Fourier transform $S(\omega)$ is complex and can be written in rectangular form as

$$S(\omega) = S_{real}(\omega) + iS_{imag}(\omega) \, , \tag{3}$$

where $S_{real}(\omega)$ is the real component of $S(\omega)$ and $S_{imag}(\omega)$ is the imaginary component of $S(\omega)$.

The rectangular form shown in equation (3) can be re-written in polar form as

$$S(\omega) = |S(\omega)|e^{\varphi(\omega)}, \tag{4}$$

where $|S(\omega)|$ = the amplitude spectrum, and $\varphi(\omega)$ = the phase spectrum, of $s(t)$.

In their discrete form, the Fourier transform pair given in equations (1) and (2) are fundamental to all aspects of seismic signal processing, from frequency filtering through to seismic migration. However, Gabor (1946) noticed two fundamental problems with the Fourier transform:

(1) For perfect reconstruction of the forward and inverse transforms, an infinite signal length is required, which is never satisfied in observed signals.

(2) As indicated in equations (3) and (4), the time signal is real but the frequency signal is complex.

To solve the first problem, and motivated by Heisenberg's uncertainty principle, Gabor proposed a time-frequency "quantum" of information which satisfied $\Delta t \Delta f \approx 1.0$. That is, he proposed creating a grid of squares in time-frequency space as shown in Figure 1, where the basic "quantum" of information is shown by the red square of dimension Δt by Δf.

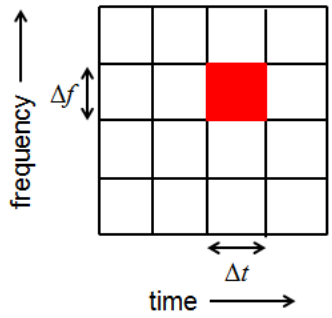

Figure 1. Gabor's concept of the time-frequency "quantum" of information. (adapted from Gabor, 1947).

For the "elementary signal" within each square, Gabor chose a sinusoidal function modulated by a Gaussian envelope. A pictorial representation of Gabor's "elementary signal" is shown in Figure 2, where the cosine is the real part of the signal and the sine is the imaginary part.

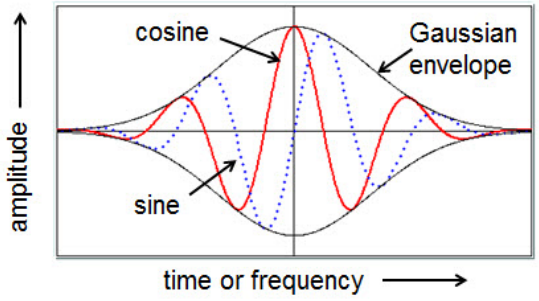

Figure 2. The Gabor wavelet.

The wavelet pair shown in Figure 2 is now called the complex Gabor wavelet in wavelet transform theory, and can be considered to be one of the starting points for the development of wavelet transforms. Gaussian modulation of the Fourier transform lead to the development of Gabor transform, whose use has been well documented by Dr. Margrave. For the rest of this report, I will thus concentrate of Gabor's solution to the second problem posed above (i.e. the time and frequency signals are miss-matched, since one is real and the other is complex), which will lead us to seismic attributes.

THE COMPLEX SIGNAL

Gabor next went on to the second problem: how do we create a complex time signal, of which the observed signal is the real component? Since the Fourier transform of a real signal has a symmetric shape on both the positive and negative frequency side, Gabor proposed that to do this we simply need to suppress the amplitudes belonging to negative frequencies, and multiply the amplitudes of the positive frequencies by two. To compute the form of the complex signal using this approach requires the evaluation of an improper integral. However, in his paper Gabor (1946) states that it can be "easily verified" that the solution is

$$z(t) = s(t) + ih(t), \tag{5}$$

where $i = \sqrt{-1}$, $z(t)$ = the complex signal, and $h(t)$ = the Hilbert t ransform of $s(t)$.
Details of the solution are found in Gabor (1946) and Cohen (1995). The signal $z(t)$ is also often called the analytic signal because it must satisfy the Cauchy-Riemann conditions for differentiability, which puts it in a class of functions which have traditionally been called analytic. As Cohen (1995) points out, there are an infinite number of possibilities for the form of the imaginary component of the complex signal, since we only measure the real part. Although we will not go into the details here, Cohen's main argument in favour of this approach is that Gabor's intuition in zeroing out the negative parts of the frequency spectrum means that the average frequency is now at the centre of the amplitude spectrum defined in equation (4), rather than being at zero (which it is when we have symmetric positive and negative frequency parts of the spectrum).

To physically interpret equation (5), note that the Hilbert transform is a filter which applies a 90^o phase shift to every sinusoidal component of a signal. The complex trace can be transformed from the rectangular form given in equation (5) to polar coordinates, to give the instantaneous amplitude envelope $A(t)$ and instantaneous phase $\Phi(t)$ given by

$$z(t) = A(t)e^{i\Phi(t)} = A(t)\cos\Phi(t) + iA(t)\sin\Phi(t), \tag{6}$$

where $A(t) = \sqrt{s(t)^2 + h(t)^2}$ and $\Phi(t) = \tan^{-1}\left[\frac{h(t)}{s(t)}\right]$. I have given the instantaneous phase a different symbol than the frequency phase in equation (4) ($\Phi(t)$ versus $\phi(\omega)$) to clearly differentiate between these two different phase terms.

The complex trace was introduced into geophysics by Taner et al. (1979), who also discussed its digital implementation and introduced the term "seismic attribute" into exploration geophysics. As well as introducing the amplitude envelope and instantaneous phase attributes, Taner et al. (1979) also introduced the instantaneous frequency of the complex seismic trace as an attribute, which was initially derived by J. Ville (1948), a paper directly inspired by Gabor (1947). The instantaneous frequency is the time derivative of the instantaneous phase, and is given in one of two ways as

$$\omega(t) = \frac{d\Phi(t)}{dt} = \frac{d\,\tan^{-1}\left(h(t)/s(t)\right)}{dt} = \frac{s(t)\frac{dh(t)}{dt} - h(t)\frac{ds(t)}{dt}}{A(t)^2}. \qquad (7)$$

The reason that it is preferable to use the second approach, which involves derivatives of both the seismic trace and its Hilbert transform, is that the instantaneous phase "wraps-around" at + and – π, and therefore is unsuitable for differentiation. Like the Hilbert transform, the derivative applies a 90° phase shift, but it also applies a high frequency ramp in the frequency domain. The derivative operation can be performed either in the frequency domain or with a $2M$+1 length temporal filter (Fornberg, 1987).

To illustrate the various attribute methods, Figure 3 shows a 3D seismic volume that was recorded over a karsted terrain (Hardage et al., 1996). It consists of 97 inlines and 133 crosslines, each with 200 samples (800–1200 ms). The karst features are illustrated by the red ellipses.

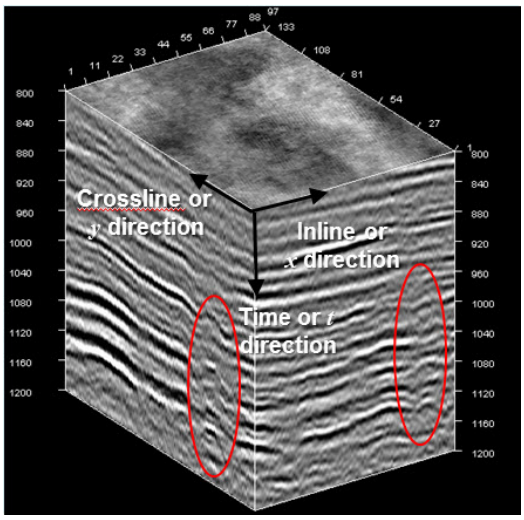

Figure 3. The seismic volume that will be used to illustrate our attribute methods, where the red ellipses indicate karst features.

Figures 4 and 5 are displays of vertical and horizontal slices through the seismic volume shown in Figure 3. In particular, notice the karst feature on the right side of the seismic line in Figure 4, which can also be seen as an elliptical contour on the time slice in Figure 5.

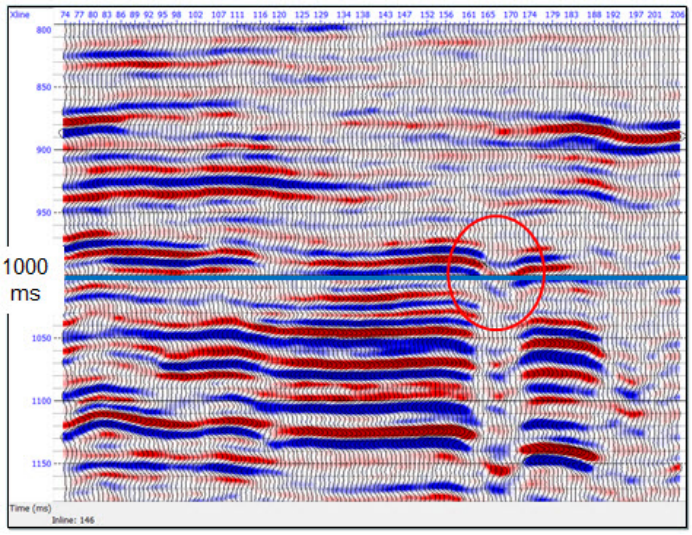

Figure 4. Seismic inline 146 taken from the seismic volume shown in Figure 3, where the red ellipse indicates a karst feature. A 1000 ms time slice is shown in the next figure.

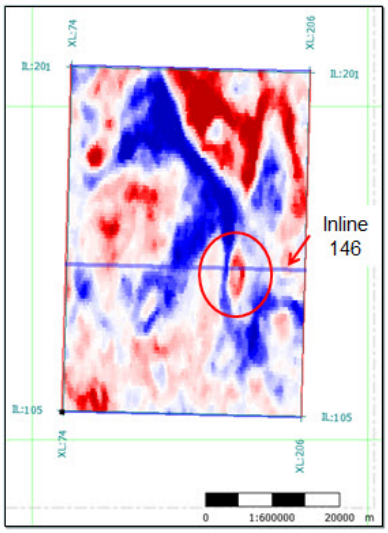

Figure 5. A 1000 msec time slice cut from the seismic volume shown in Figure 3, where inline 146 is shown on the display and the red ellipse indicates a karst feature.

Figure 6 is a display of the instantaneous attributes associated with the seismic amplitude slice at 1000 msec, where Figure 6(a) shows the amplitude envelope slice, Figure 6(b) shows the instantaneous phase slice, and Figure 6(c) shows the instantaneous frequency slice. Notice that the karst feature is best seen on the instantaneous phase slice.

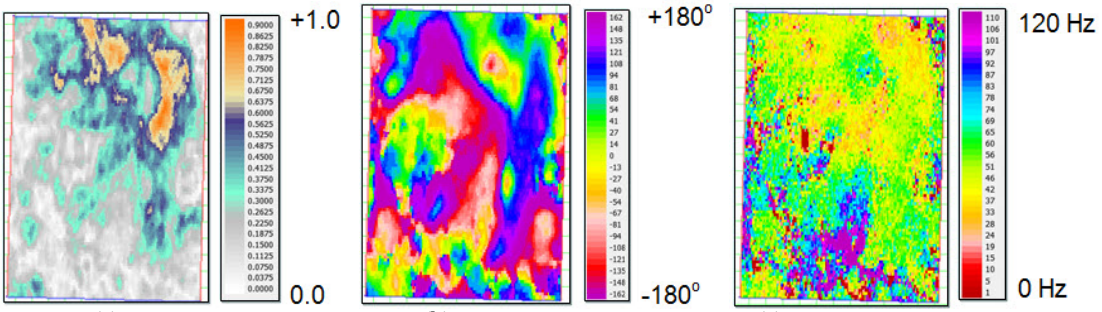

Figure 6. Instantaneous attributes derived from the 1000 msec time slice shown in Figure 5, where (a) shows instantaneous amplitude, (b) shows instantaneous phase, and (c) shows instantaneous frequency.

CORRELATION-BASED ATTRIBUTES

Attribute analysis until the mid-1990s was based on the three basic attributes introduced by Gabor and Ville in the 1940s: instantaneous phase, instantaneous frequency and instantaneous amplitude. Then, in the space of roughly ten years, papers on two new approaches to attribute analysis appeared, both based on cross-correlations between traces. The coherency method (Bahorich and Farmer, 1995) was a new approach which relied on computing cross-correlation coefficients between traces. Several extensions to coherency were then published: the semblance method (Marfurt et al., 1998) and the eigen-coherence method (Gersztenkorn and Marfurt, 1999). Next, Roberts (2001) introduced curvature attributes. Although these first curvature attributes were based on a picked horizon, Klein et al. (2008) showed how they could be extended to the full seismic volume using the time shifts from a trace-to-trace correlation. It was hard to see how instantaneous attributes and coherency and curvature based on cross correlation were related. However, the link was provided in the paper by Barnes (1996) on 2-D and 3-D complex trace analysis, which will be discussed in the next section. Let us first discuss the correlation-based attributes.

First, we will discuss the coherency approach. The coherency method and the related methods of semblance and eigen-coherency are based of first computing a coherency matrix from a rolling window of J traces and $2M+1$ samples, as shown in Figure 7a. If we search over a range inline and crossline dips p and q, as shown in Figure 7b, the full coherency matrix can be written as

$$C(p,q) = \begin{bmatrix} c_{11} & \dots & c_{1J} \\ \vdots & \ddots & \vdots \\ c_{J1} & \dots & c_{JJ} \end{bmatrix}, \tag{8}$$

where $c_{ij} = \sum_{t=-M\Delta t}^{M\Delta t} s_i(t - px_i - qy_i)s_j(t - px_j - qy_j)$. Let us now look at how this coherency matrix is used in the three methods described above.

The first coherency method (Bahorich and Farmer, 1995) involved finding the maximum correlation coefficients between adjacent traces in the *x* and *y* directions, and taking their harmonic average, which can be written (Marfurt et al., 1999) as

$$coh_1 = \max\left[\left(\frac{c_{12}}{(c_{11}c_{22})^{1/2}}\frac{c_{13}}{(c_{11}c_{33})^{1/2}}\right)^{1/2}\right]. \tag{9}$$

Marfurt et al. (1998) extended this by computing the semblance of all combinations of all *J* traces in the window in Figure 7a. This can be written mathematically as

$$coh_2 = \max\left[\frac{a^T C(p,q)a}{Tr[C(p,q)]}\right]. \tag{10}$$

where $a^T = [1, \ \ldots, \ 1]$ and $Tr[C(p,q)] =$ sum of main diagonal of $C(p,q)$.

The third approach, eigen-coherency (Gersztenkorn and Marfurt, 1999), involves finding the maximum eigenvalue of *C*(*p*,*q*) and dividing by the sum of the eigenvalues, and can be written

$$coh_3 = \max\left[\lambda_1 / \sum_{j=1}^{j} \lambda_j\right], \tag{11}$$

where $\lambda_i, i = 1, \ldots, J$ are the eigenvalues of *C*(*p*,*q*). Note that it can be shown mathematically that the trace of *C*(*p*,*q*), which is the sum of the main diagonal, is identical to the sum of the eigenvalues of *C*(*p*,*q*), or *Tr*[*C*(*p*,*q*)]. Thus, the denominators in equations (10) and (11) are actually equivalent to each other. Although the formulation of eigen-coherency given in the paper by Gersztenkorn and Marfurt (1999) did not search over dip angles *p* and *q*, an algorithm that did this was introduced by Marfurt et al. (1999).

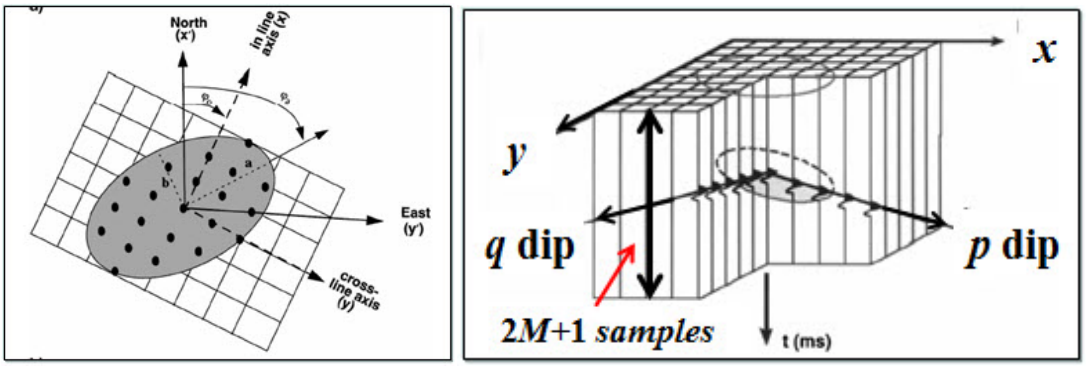

(a) (b)

Figure 7. Search criteria for coherency methods, where (a) shows an elliptical spatial window with *J* traces used to extract the cross-correlations, and (b) shows the dip searches *p* and *q* over the 2M+1 sample time window (from Marfurt, 2006)

Figure 8 shows an example of coherency computed over the full Boonsville data cube, where the 1000 msec time slice has been extracted. The algorithm used

was eigen-coherency with no dip scans. Notice the excellent definition of the karst feature, which is outlined by a red ellipse.

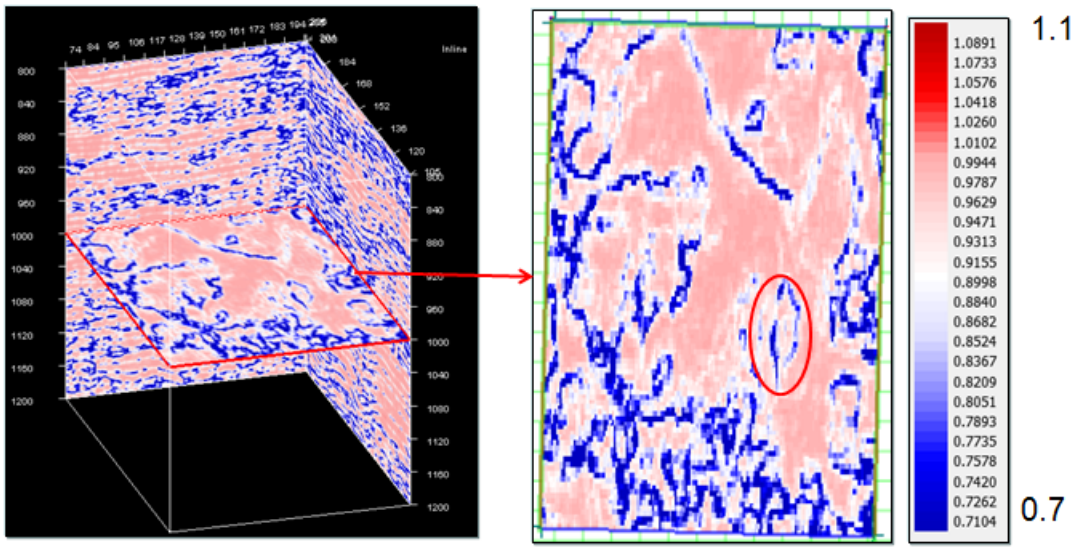

Figure 8. Eigen-coherency applied to the Boonsville data cube, where the 1000 msec time slice is shown on the right. Notice the excellent definition of the karst feature, as highlighted with the red ellipse.

Let us now move from coherency to curvature. Roberts (2001) shows that curvature can be estimated from a time structure map by fitting the local quadratic surface given by

$$t(x, y) = ax^2 + by^2 + cxy + dx + ey + f \ . \qquad (12)$$

Note that this equation is a combination of an ellipsoid (the first three terms) and a dipping plane (the last three terms), as illustrated in Figure 9. Also, the coefficients *d* and *e* are identical to the inline and crossline dips *p* and *q* defined earlier for the coherency searches.

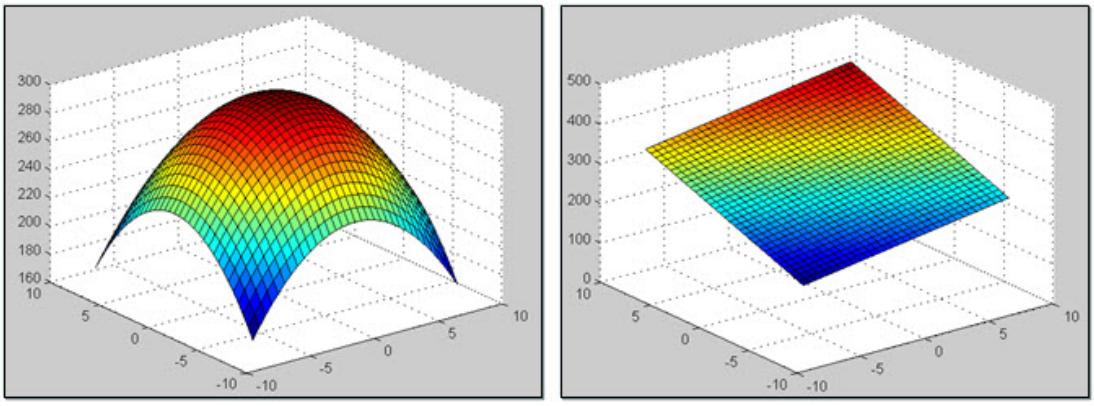

Figure 9. Equation (12) is a combination of the ellipsoid shown on the left (terms *a*, *b* and *c*) and the dipping plane shown on the right (terms *d*, *e* and *f*).

Roberts (2001) shows that at each *x* and *y* location, the coefficients *a* through *f* can be estimated from the three-by-three grid of time structure points shown in Figure 10.

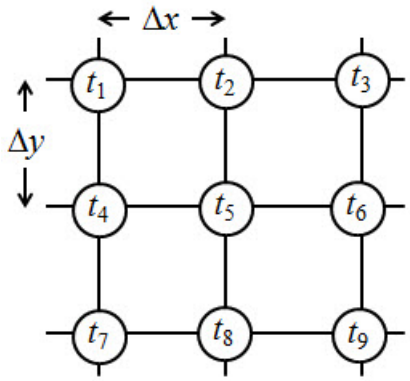

Figure 10. The three-by-three rolling window of seismic time picks used by Roberts (2001) as a way to compute the curvature coefficients given in equation (12).

For example, coefficient *d* is estimated by:

$$d = \frac{\partial t}{\partial x} = \frac{(t_3 + t_6 + t_9) - (t_1 + t_4 + t_7)}{2\Delta x}. \tag{13}$$

For the computations of the other coefficients refer to Roberts (2001). Note also that the time shifts on the grid in Figure 10 do not have to come from a picked surface. To generalize this method to a complete seismic cube, Klein et al. (2008) proposed computing the time shifts from the shift at the maximum correlation coefficient between the central trace of the grid and the other traces. This would make t_5 equal to zero. Thus, curvature can be seen of as a related correlation attribute to coherence, where coherence is based on the correlation coefficient and curvature is based on the correlation time shift.

The two curvature attributes proposed by Roberts (2001) that are the easiest to visualize are K_{max} and K_{min}, which can be written mathematically as

$$K_{\max} = K_{mean} + \sqrt{K_{mean}^2 - K_{gauss}}, \tag{14}$$

and

$$K_{\min} = K_{mean} - \sqrt{K_{mean}^2 - K_{gauss}}, \tag{15}$$

where $K_{gauss} = \frac{4ab - c^2}{(1 + d^2 + e^2)^{1/2}}$ and $K_{mean} = \frac{a(1+e^2) + b(1+d^2) - cde}{(1 + d^2 + e^2)^{3/2}}$. Notice that we can also write K_{mean} and K_{gauss} as functions of K_{max} and K_{min}, or

$$K_{mean} = \frac{K_{\min} + K_{\max}}{2} \text{ and } K_{gauss} = K_{\min} K_{\max}.$$

A pictorial representation of the attributes K_{max} and K_{min} is shown in Figure 11, superimposed on a quadratic surface.

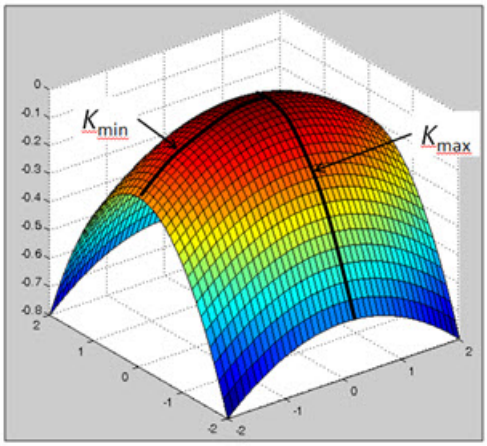

Figure 11. An illustration of the curvature attributes K_{max} and K_{min}.

Roberts (2001) also defines most positive and negative curvature K_+ and K_-, which are equal to $K_{\min}$ and $K_{\max}$ with $d = e = f = 0$. That is, we are looking at a pure ellipsoid with linear dip removed. Simplifying equations (14) and (15) gives us

$$K_+ = (a+b) + \sqrt{(a-b)^2 - c^2}\,, \tag{16}$$

and

$$K_- = (a+b) - \sqrt{(a-b)^2 - c^2}\,. \tag{17}$$

It is interesting to note that there is another way to define most positive and negative curvature attributes K_+ and K_-. Let us re-write the first three terms of equation (12) in the following equivalent form:

$$t(x,y) = \begin{bmatrix} x & y \end{bmatrix} \begin{bmatrix} a & c/2 \\ c/2 & b \end{bmatrix} \begin{bmatrix} x \\ y \end{bmatrix} = \vec{x}^T A \vec{x}\,. \tag{18}$$

Then, the eigenvalues of matrix A are given by

$$\begin{vmatrix} a-\lambda & c/2 \\ c/2 & b-\lambda \end{vmatrix} = \lambda^2 - (a+b)\lambda + (ab - c^2/4) = 0\,, \tag{19}$$

or

$$\lambda = \frac{1}{2}(a+b) \pm \sqrt{(a-b)^2 + c^2}\,. \tag{20}$$

Thus, by comparing equation (20) to equations (16) and (17), we see that the most positive and negative curvature attributes K_+ and K_- are equal to the eigenvalues of matrix A, which means that they represent the rotation of the quadratic equation (12) to its principal axes. Another way to look at this is that we remove the cross term xy.

Yet another curvature attribute is Euler curvature, written as

$$K_{euler}(\delta) = K_{\min}\cos^2\delta + K_{\max}\sin^2\delta \ , \qquad (17)$$

where δ represents an azimuth angle. Notice that most of our previous curvatures can be derived from Euler curvature:

$$K_{\min} = K_{euler}(0^o),\ K_{\max} = K_{euler}(90^o),\ K_{mean} = K_{euler}(45^o),\ K_{gauss} = K_{euler}(0^o)K_{euler}(90^o).$$

In the case where linear dip has been removed, K_+ and K_- can be substituted for $K_{\min}$ and $K_{\max}$. There are other types of curvatures defined by Roberts (2001), but the ones defined above are the most common. Figure 12 shows maximum and minimum curvature compared with the original time slice.

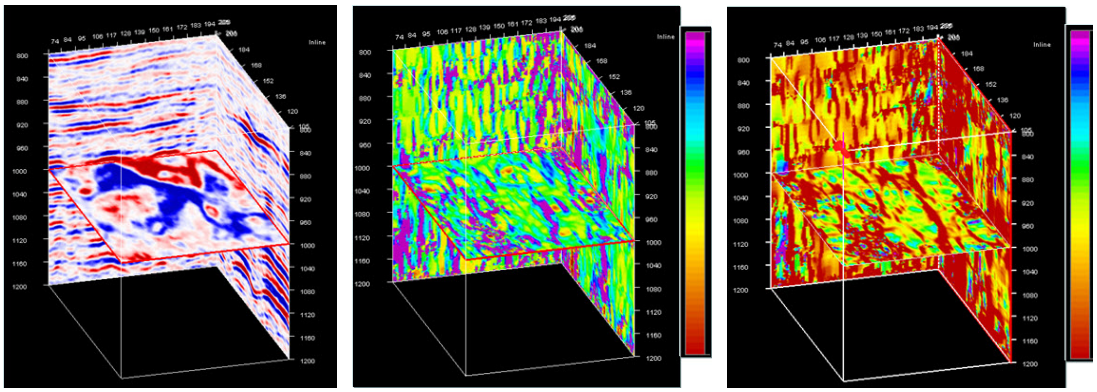

(a) (b) (c)

Figure 12. A display of curvature attributes. The 1000 msec time slice is shown in (a), maximum curvature is shown in (b) and minimum curvature is shown in (c).

INSTANTANEOUS AND CORRELATION ATTRIBUTES

At first glance, there appears to be no relationship between instantaneous attributes, coherency and curvature. However, notice that in the coherency method it is important to find the *x* and *y* dips, called *p* and *q*. Also note that the coefficients *d* and *e* in equation (12) are identical to the inline and crossline dips *p* and *q* defined. Furthermore, if we differentiate equation (12) we find that at $x = y = 0$ the first three quadratic coefficients can be written $a = \frac{1}{2}\left(\frac{\partial p}{\partial x}\right), b = \frac{1}{2}\left(\frac{\partial q}{\partial y}\right)$, and $c = \frac{1}{2}\left(\frac{\partial p}{\partial y} + \frac{\partial q}{\partial x}\right)$. Thus, we can re-write equation (12) as a function of the dips and their *x* and *y* derivatives, as follows:

$$t(x,y) = \frac{1}{2}\left(\frac{\partial p}{\partial x}\right)x^2 + \frac{1}{2}\left(\frac{\partial q}{\partial y}\right)y^2 + \frac{1}{2}\left(\frac{\partial p}{\partial y} + \frac{\partial q}{\partial x}\right)xy + px + qy + f \ , \qquad (18)$$

where the *f* term is simply a vertical shift that can be ignored. The connection between instantaneous and correlation attributes can therefore be found if we can find a connection between dip and instantaneous attributes.

This relationship was first described in a paper by Barnes (1996) that pre-dated most of the new attributes. Barnes (1996) introduced two new spatial instantaneous attributes and showed how these attributes could be used to find both the dips and the azimuth. Although Barnes (1996) was motivated by the work of Scheuer and Oldenburg (1988) on phase versus group velocity, his method takes us back full circle to Gabor (1947). To see this, let us re-visit our earlier 3D dataset, as shown again in Figure 13, and notice that we only computed the frequency attribute in the time direction. However, since the Hilbert transform is actually a function of three coordinates (i.e. $\Phi(t,x,y)$) Barnes noted that we can also compute spatial frequencies in the inline (x) and crossline (y) directions.

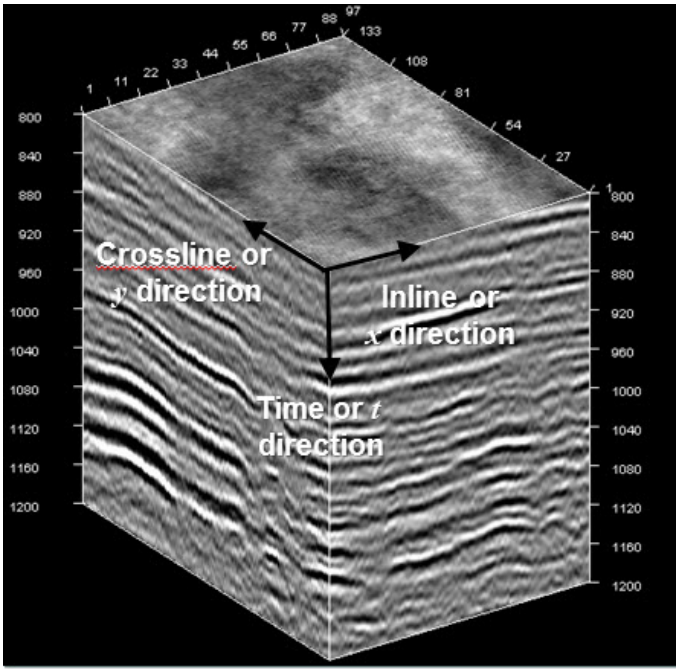

Figure 13. The 3D Boonsville seismic volume.

Analogous to instantaneous frequency, Barnes (1996) therefore defined the instantaneous wavenumbers k_x and k_y (using the Marfurt (2006) notation) as:

$$k_x = \frac{\partial \Phi(t,x,y)}{\partial x} = \frac{s\dfrac{\partial h}{\partial x} - h\dfrac{\partial s}{\partial x}}{A^2}, \tag{19}$$

and

$$k_y = \frac{\partial \Phi(t,x,y)}{\partial y} = \frac{s\dfrac{\partial h}{\partial y} - h\dfrac{\partial s}{\partial y}}{A^2}. \tag{20}$$

As with instantaneous frequency, the derivative operation can be done either in the frequency domain or using finite differencing up to a given order. The instantaneous time dips in the x and y direction, p and q, are then given as:

$$p = \frac{k_x}{\omega} = \frac{T}{\lambda_x}, \tag{21}$$

and

$$q = \frac{k_y}{\omega} = \frac{T}{\lambda_y}, \tag{22}$$

where T = period and λ = wavelength. Using the dips p and q, the azimuth ϕ and true time dip θ are then given by:

$$\phi = \tan^{-1}(p/q) = \tan^{-1}(k_x/k_y), \tag{23}$$

and

$$\theta = \sqrt{p^2 + q^2}\ . \tag{24}$$

To understand this concept, I created a seismic volume that consisted of a dipping cosine wave, which is shown in Figure 14. The period, wavelength and time dip are shown on the plot, where the period is found by measuring the time between successive peaks, and the wavelength from the picked horizon.

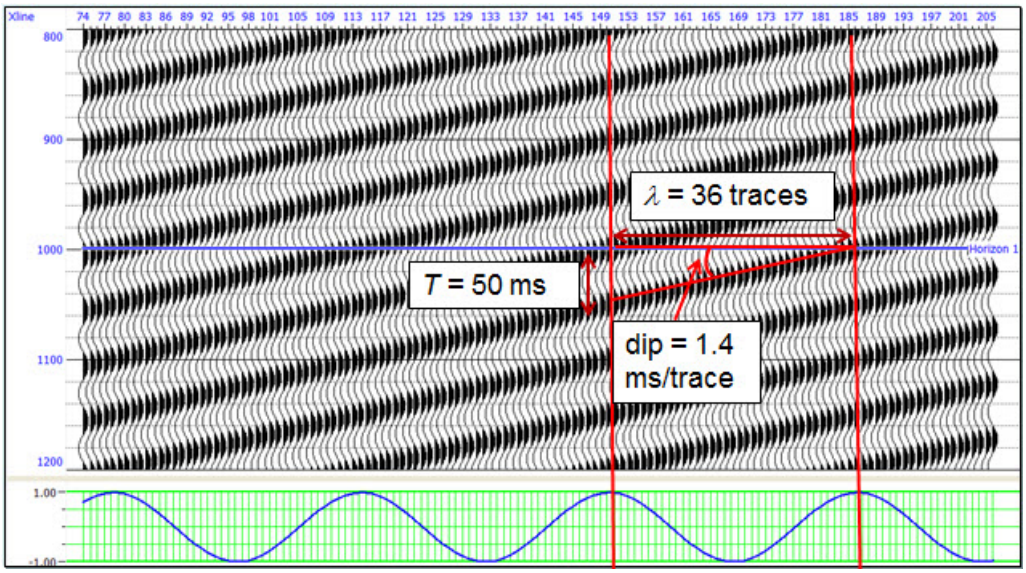

Figure 14. A dipping cosine wave with the period and wavelength illustrated. Note that the dip is given by the period/wavelength.

Next, let's look at the dipping cosine wave in 3D, as shown in Figure 15. In this display, we have sliced it along the x, y and time axes. For this dipping event, it is clear how the dips and azimuths are related to the instantaneous frequency and wavenumbers. Note that in this example, the p dip is steeper than the q dip, so the true dip, which is found along a line which is orthogonal to strike, we be computed from equation (24).

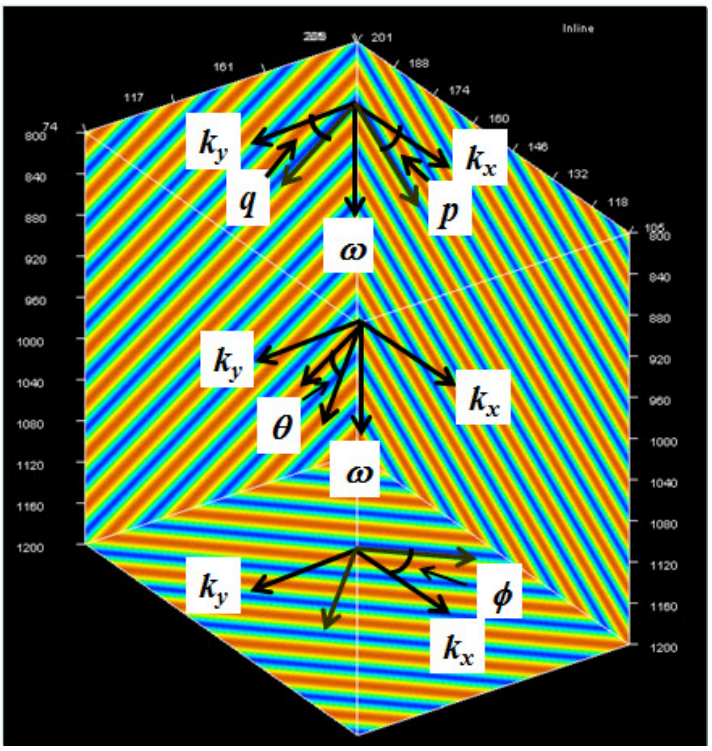

Figure 15. A dipping cosine wave in 3D, where the inline and crossline dips p and q are illustrated, as well as the true dip θ and azimuth ϕ.

Next, we will illustrate these instantaneous spatial attributes using the Boonsville dataset. There are many possible displays based on the "building blocks" for these attribute, which include the derivatives of seismic amplitude, Hilbert transform and phase in the t, x, and y directions, the three frequencies, and p, q, true dip and azimuth. Note that the many divisions involved in the computations make this method very sensitive to noise when compared to correlation based methods. In Figure 16, the true dip and azimuth are compared with the time slice from the Boonsville dataset.

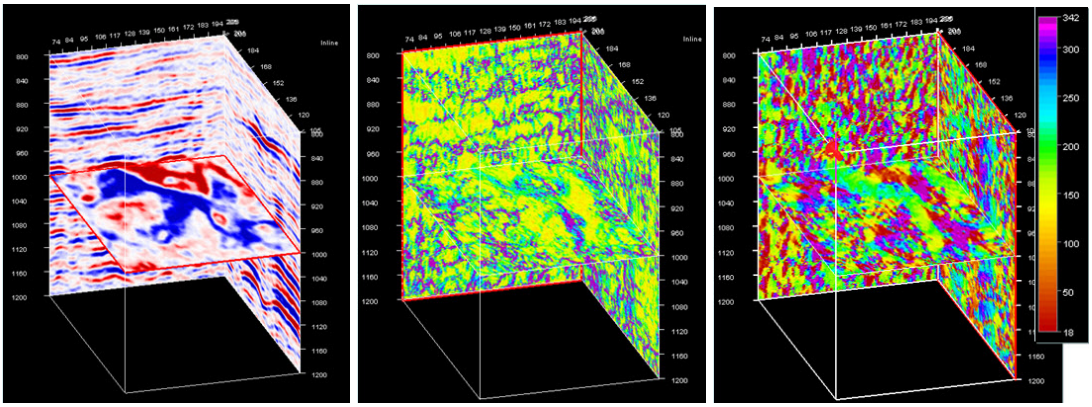

(a) (b) (c)

Figure 16. A display of instantaneous dip and azimuth attributes, where the 1000 msec time slice is shown in (a), instantaneous dip is shown in (b) and instantaneous azimuth is shown in (c).

Note that as part of the correlation curvature method, azimuth can also be estimated if we replace the *p* dip attribute by coefficient *d* in equation (12) and the *q* attribute by coefficient *e* in equation (12), and then use equation (24) to compute azimuth. A comparison between the two azimuth methods is shown in Figure 17, where we see good similarity between the two plots, but higher frequency detail in the instantaneous azimuth calculation.

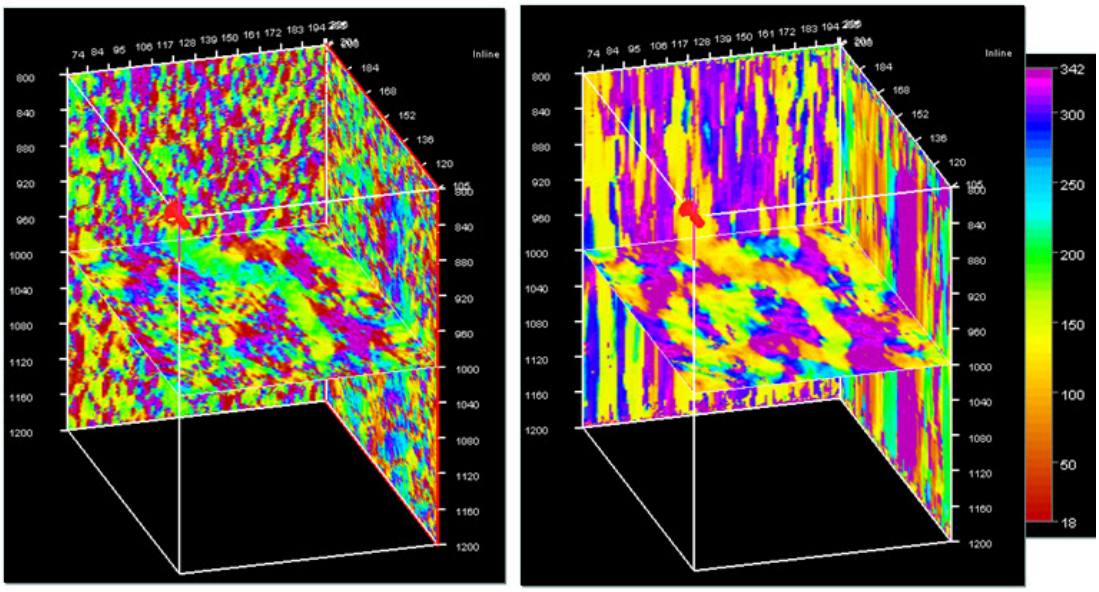

(a) (b)

Figure 17. A comparison of instantaneous azimuth and correlation azimuth attributes, where instantaneous azimuth is shown in (a), and correlation azimuth is shown in (b). The time slice displayed in the plot is at 1000 msec.

Also, recall from equation (18) that all of the curvature attributes can be derived from the instantaneous dip attributes described earlier, using a second differentiation, as was observed by al-Dossary and Marfurt (2006). Figure 18 shows a comparison between maximum curvature derived the two different ways, where Figure 18 (b) shows instantaneous maximum curvature and Figure 18 (c) shows correlation maximum curvature. The two different curvature methods give similar results. However, although instantaneous curvature shows a higher frequency lineament than correlation curvature, as shown by the ellipses, it misses the feature shown by the circles which the correlation curvature captured. Thus, each method has its own strengths.

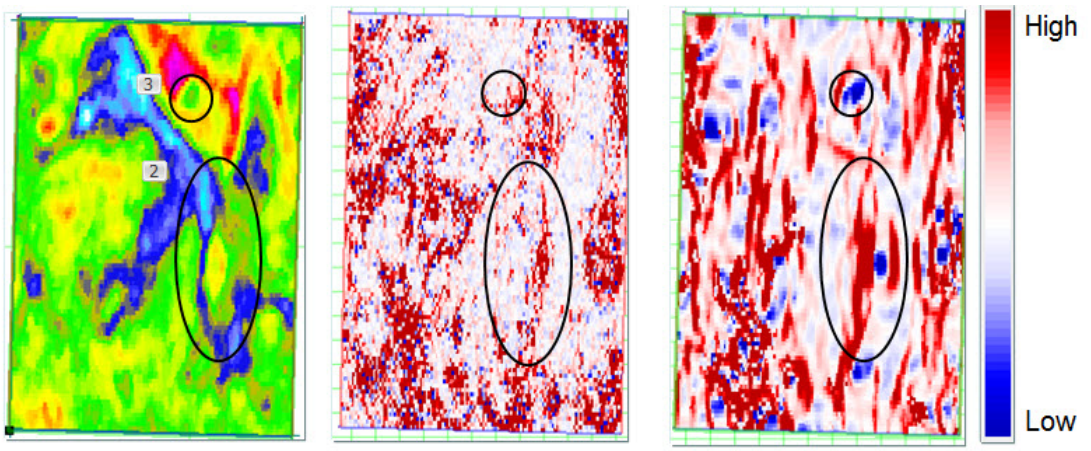

(a) (b) (c)

Figure 16. A display of maximum curvature attributes computed using instantaneous and correlation methods, where the 1000 msec time slice is shown in (a), instantaneous maximum curvature is shown in (b) and correlation maximum curvature is shown in (c). Note that the colour scale on (c) is different than the colour scale used on this plot in Figure 12 b. The ellipses show a lineament feature and the circles show circular feature.

CONCLUSIONS

In this report, I have shown how Dennis Gabor can justifiably be considered as the father of seismic attribute analysis, based on his invention of the complex signal (Gabor, 1947). I have also provided an historical overview of seismic attributes and shown their inter-relationships.

The introduction of the complex signal by Gabor lead to the development of the first set of seismic attributes by Taner et al. (1979). These initial attributes were restricted to complex amplitude, phase and frequency in the time direction. More recent attributes such as coherency (Bahorich and Farmer, 1995) and curvature (Roberts, 2001) at first appeared unrelated to the instantaneous attributes. However, as shown by Barnes (1996) and Marfurt (2006), by extending Gabor's concept of the complex signal to the *x* and *y* directions in a seismic volume, the dip, azimuth and curvature attributes can all be computed. These new attributes are actually higher in frequency content than the original correlation versions. Although there appears to be no direct connection between coherency and instantaneous attributes, the dip steering done as part of the coherency process can be done using instantaneously derived dips.

REFERENCES

al-Dossary, S., and K. J. Marfurt, 2006, 3D volumetric multispectral estimates of reflector curvature and rotation: Geophysics, **71**, 41–51.

Bahorich, M. S., and S. L. Farmer, 1995, 3-D seismic discontinuity for faults and stratigraphic features, The coherence cube: The Leading Edge, **16**, 1053–1058.

Barnes, A. E., 1996, Theory of two-dimensional complex seismic trace analysis: Geophysics, **61**, 264–272.

Cohen, L., 1995, Time-Frequency Analysis: Prentice-Hall PTR.

Fornberg, B., 1987, The pseudospectral method: Comparisons with finite differences for the elastic wave equation: Geophysics, 52, 483-501.

Gabor, D., 1946, Theory of communication, part I: J. Int. Elect. Eng., v. 93, part III, p. 429-441.

Gersztenkorn, A., and K. J. Marfurt, 1999, Eigenstructure based coherence computations as an aid to 3D structural and stratigraphic mapping: Geophysics, **64**, 1468–1479.

Klein, P., L. Richard and H. James, 2008, 3D curvature attributes: a new approach for seismic interpretation: First Break, 26, 105–111.

Marfurt, K. J., 2006, Robust estimates of 3D reflector dip: Geophysics, 71, 29-40.

Marfurt, K. J., and R. L. Kirlin, 2000, 3D broadband estimates of reflector dip and amplitude: Geophysics, **65**, 304–320.

Marfurt, K. J., R. L. Kirlin, S. H. Farmer, and M. S. Bahorich, 1998, 3D seismic attributes using a running window semblance-based algorithm: Geophysics, **63**, 1150–1165.

Marfurt, K. J., V. Sudhakar, A. Gersztenkorn, K. D. Crawford, and S. E. Nissen, 1999, Coherency calculations in the presence of structural dip: Geophysics **64**, 104–111.

Margrave, G.F, Henley, D.C., Lamoureux, M.P., Iliescu, V. and Grossman, J.P., 2002, An update on Gabor deconvolution: CREWES Research Report, Volume 14.

Roberts, A., 2001, Curvature attributes and their application to 3D interpreted horizons: First Break, 19, 85–100.

Taner, M. T., F. Koehler, and R. E. Sheriff, 1979,Complex seismic trace analysis: Geophysics, **44**, 1041–1063.

Ville, J., 1948, Théorie et applications de la notion de signal analytique: Laboratoire de Télécommunications de la Société Alsacienne de Constructions Mécaniques.

ACKNOWLEDGEMENTS

We wish to thank our colleagues at the CREWES Project and at CGGVeritas and Hampson-Russell for their support and ideas, as well as the sponsors of the CREWES Project.